Journal of Materials Chemistry A

ROYAL SOCIETY OF CHEMISTRY

PAPER

View Article Online
View Journal | View Issue

Cite this: J. Mater. Chem. A, 2024, 12, 13281

Insights from experiment and machine learning for enhanced TiO_2 coated glazing for photocatalytic NO_x remediation†

Zhi-Peng Lin,*[a] Yuankai Li,[a] Saif A. Haque,[a] Alex M. Ganose[ab] and Andreas Kafizas[ac]

In this study, 58 distinct TiO_2-coated glass samples were synthesized *via* Atmospheric Pressure Chemical Vapour Deposition (APCVD) under controlled synthesis conditions. The crystal properties, optical properties, surface properties and photogenerated charge carrier behaviour of all synthesized samples were characterized by X-ray diffraction (XRD), UV-visible spectroscopy, atomic force microscopy (AFM), and transient absorption spectroscopy (TAS), respectively. The photocatalytic activity of all coatings was systematically assessed against NO gas under near-ISO (22 197-1:2016) test conditions. The most active TiO_2 coating showed ~22.3% and ~6.6% photocatalytic NO and NO_x conversion efficiency, respectively, with this being ~60 times higher than that of a commercial self-cleaning glass. In addition, we compared the accuracy of different machine learning strategies in predicting photocatalytic oxidation performance based on experimental data. The errors of the best strategy for predicting NO and NO_x removal efficiency on the entire data set were ±2.20% and ±0.92%, respectively. The optimal ML strategy revealed that the most influential factors affecting NO photocatalytic efficiency are the sample surface area and photogenerated charge carrier lifetime. We then successfully validated our ML predictions by synthesising a new, high-performance TiO_2-coated glass sample in accordance with our ML simulated data. This sample performed better than commercially available self-cleaning glass under a new metric, which comprehensively considered the visible light transmittance (VLT), NO degradation rate and NO_2 selectivity of the material. Not only did this research provide a panoramic view of the links between synthesis parameters, physical properties, and NO_x removal performance for TiO_2-coated glass, but also showed how ML strategies can guide the future design and production of more effective photocatalytic coatings.

Received 26th February 2024
Accepted 5th April 2024

DOI: 10.1039/d4ta01319k

rsc.li/materials-a

1 Introduction

Nitrogen and oxygen are two of the most abundant gases in the atmosphere. Combustion processes often result in the formation of nitrogen oxides (represented by NO and NO_2 and known together as NO_x), where anthropogenic activities have significantly increased global emissions over the past two centuries from 0 to ~25 TgN (tera-grams of nitrogen) per year.[1,2] Vehicular emissions and chemical combustion (in particular from thermal power plants) are the main contributors to escalating NO_x levels.[3] In order to limit and reduce NO_x emissions from its source, a variety of strategies have been explored over the past few decades, including the development of NO_x adsorbent materials[4,5] and automotive three-way catalytic converters.[6,7] Alongside these efforts, lawmakers around the world have strengthened legislative measures.[8,9] For instance, guided by the Convention on Long-range Transboundary Air Pollution (CLRTAP) and the National Emissions Cap Regulation (NECR), the UK government promised to reduce NO_2 emissions to 73% of 2005 levels by 2030.[10] Despite these efforts, the annual growth rate of global NO_x emissions has not decreased and remains from 2 to 8 TgN per year.[11] These NO_x emissions pose a great threat to humans, animals, and plant ecosystems.[9,12]

To lower NO_x emissions in the air, one emerging strategy is to use photocatalysts that can oxidise NO_x emissions to more benign nitrates. This technology often involves the application of the semiconductor photocatalyst titanium dioxide (TiO_2) onto a variety of building materials, such as concrete,[13] ceramics,[14] and glass,[15,16] resulting in so-called "self-cleaning surfaces".[17] The selection of TiO_2 is not only due to its high hydrophilicity, which contributes to the self-cleaning effect, but also because TiO_2 has been one of the most successful photo-responsive materials to date, which has been widely employed

[a]Department of Chemistry, Molecular Science Research Hub, Imperial College London, White City, London, W12 0BZ, UK. E-mail: a.ganose@imperial.ac.uk; a.kafizas@imperial.ac.uk

[b]Thomas Young Centre, The London Centre for the Theory and Simulation of Materials, Royal School of Mines, Imperial College London, South Kensington, London, UK

[c]London Centre for Nanotechnology, Imperial College London, SW7 2AZ, UK

† Electronic supplementary information (ESI) available. See DOI: https://doi.org/10.1039/d4ta01319k

in photocatalytic indoor environmental remediation[18] and in other photo-electron applications such as energy storage.[19,20]

A typical process of employing self-cleaning surfaces in NO_x photocatalytic degradation is shown and described in Fig. S1† and eqn (1)–(7). In detail, when TiO_2 is exposed to ultra-bandgap light, electrons are excited from its valence band (VB) to its conduction band (CB). The electrons in the CB (e_{cb}^-) can reduce oxygen in the air and form superoxide radicals (O_2^-), which react with NO and a proton to produce nitric acid (HNO_3). Meanwhile, the holes in the VB (h_{vb}^+) can oxidise water to produce hydroxyl radicals (OH*), which undergo a series of chemical reactions to produce HNO_3. The resulting HNO_3 can be easily rinsed off by rainwater, ensuring safe removal into the urban drainage system when applied in cities.[21,22]

$$TiO_2 + h\nu \rightarrow e_{cb}^- + h_{vb}^+ \quad (1)$$

$$H_2O + h_{vb}^+ \rightarrow H^+ + OH^* \quad (2)$$

$$e_{cb}^- + O_2 \rightarrow O_2^- \quad (3)$$

$$O_2^- + NO + H^+ \rightarrow HNO_3 \quad (4)$$

$$NO + OH^* \rightarrow HONO \quad (5)$$

$$HONO + OH^* \rightarrow NO_2 + H_2O \quad (6)$$

$$NO_2 + OH^* \rightarrow HNO_3 \quad (7)$$

Many studies have validated the effectiveness of employing TiO_2 for NO_x remediation in a range of building materials. For example, in 2009, Hüsken *et al.*[23] reported that TiO_2 modified concrete was able to achieve up to ~39% NO_x removal efficiency using ISO test conditions. In 2014, Ângelo *et al.*[24] noted a ~70% NO conversion under ISO test conditions with a TiO_2-enhanced paint using Cristal ACTiV™ PC500. And in 2016, Wang *et al.*[25] showed that TiO_2-modified asphalt was able to convert ~67% of NO under ISO test conditions also.

With regard to glass, the photocatalytic NO_x removal efficiency of TiO_2-coated windows has rarely been reported, and where it has been, has tended to show lower NO conversion levels compared with other building materials.[16,26,27] Although this indicates that further optimisation is required to produce TiO_2-coatings on windows with enhanced photocatalytic NO_x removal efficiency, it has been proposed that this lower observed performance may be compounded by the intrinsically smooth and low surface roughness of window glass.[26] Although windows were one of the first building materials to be coated with TiO_2 for photocatalytic purposes,[28] to date, it has been marketed for general purpose self-cleaning, and not specifically for remediating NO_x.[29] As a result, the potential to use TiO_2-coated windows for NO_x remediation is a largely under-explored topic and necessitates further research. Nevertheless, when developing photocatalytic coatings for windows, one should bear in mind the strict optical requirements for general purpose applications of windows, in that they should retain a high visible light transparency and maintain low haze.

TiO_2 coatings on window glass are commercially produced using atmospheric pressure chemical vapour deposition (APCVD).[29] Typically, APCVD utilizes low boiling point precursors and complex conditions to control the properties of the coating on the substrate. Many synthetic variables of the APCVD process, such as deposition temperature and synthesis time, can affect the physicochemical properties and photocatalytic efficiency of the coating formed. For example, Nolan *et al.*[30] found that increasing the deposition temperature reduced the average particle size in the TiO_2 coating from ~84 nm at 500 °C to ~37 nm at 900 °C. In addition, Cabrera Quesada-Cabrera *et al.*[31] highlighted that altering the carrier gas flow rate can result in changes in coating thickness, with thicker films tending to exhibit greater photocatalytic activity.

Herein, we applied APCVD to synthesize TiO_2-coated glass, varying the synthetic parameters in a systematic manner to produce 58 distinct samples. These parameters included our precursor choice, deposition temperature, synthesis time, and precursor bubbler temperature. A comprehensive analysis of their impact on the physicochemical properties of the TiO_2 coatings was carried out, which included the measurement of the average crystal size, optical bandgap, surface roughness, and photogenerated charge carrier behaviour (population and decay kinetics) and photocatalytic NO_x activity. It is also worth noting that this research is the first to explore the links between APCVD synthesis parameters, TiO_2 coating properties, and photocatalytic NO_x conversion efficiency.

Machine Learning (ML) is an efficient and popular tool that is able to reveal complex non-linear correlations between poly-dimensional data (>5 dimensions) and make precise predictions beyond the scope of existing experimental data.[32,33] Compared to traditional optimisation and analysis methods, such as orthogonal methods, ML algorithms can handle larger datasets with more intricate interactions, and offers a more comprehensive understanding of the statistical relationships among all tested and measured features. Recent academic reviews have highlighted the successful application of ML in high-performance photocatalyst discovery,[34,35] demonstrating its advantage in identifying novel materials and optimizing synthesis conditions with a higher degree of accuracy and efficiency compared to traditional experimental design approaches. Herein, based on the data set obtained from the experiments in this article, we compared the accuracy and robustness of various ML strategies for predicting the photocatalytic NO_x performance of TiO_2-coatings on window glass from the APCVD synthetic parameters chosen and physicochemical properties measured. Using the optimal ML strategies, we were able to work backwards and gain insight into the physicochemical properties that influence photocatalytic activity the most. Considering the general purpose requirements when developing photocatalytic coatings for windows, (*i.e.*, in that they should maintain high visible light transparency and low haze), this paper establishes a new metric that considers both the visible light transmission and photocatalytic activity of the sample. Importantly, this metric was used to validate our ML predictions, where a new TiO_2-coated glass

sample was grown in accordance with these predictions and showed a high performance in this metric.

It is worth noting that this article marks the first study to systematically explore the relationships between APCVD synthesis parameters, TiO_2 coating properties, and photocatalytic NO_x conversion efficiency using ML strategies. We believe that this novel approach will not only provide pivotal guidance on the future industrial production of TiO_2 coatings on window glass for photocatalytic NO_x remediation, but also provide a more general approach to the optimisation of photocatalytic active thin films for a range of processes.

2 Experimental

2.1 Glass substrate pre-treatment

In a typical process, barrier glass (5 cm × 10 cm × 0.22 cm) with an additional one-side SiO_2 coating to avoid ion diffusion was selected as the coating substrate.[36] The glass was then successively cleaned using a diluted detergent solution (50 vol% detergent: 50 vol% water, Teepol®), followed by rinses with deionised water, acetone (Reagent Grade, BDH Chemicals UK), and isopropanol (Reagent Grade, BDH Chemicals, UK). Each cleaning step was carried out under an ultrasonic environment for 10 min to remove surface dust and organic solvents. The cleaned glass substrates were dried using a nitrogen flow and subsequently positioned at the distal end of the CVD apparatus, as illustrated in Fig. S2(a).†

2.2 APCVD synthesis of TiO_2 coatings on glass

TiO_2 coating on glass was achieved by thermal decomposition of low boiling-point Ti- precursors using APCVD (Fig. S2(a)†). Titanium *tert*-isopropoxide (TTIP, 97%, Sigma-Aldrich), titanium *n*-butoxide (TiBu, 97%, Sigma-Aldrich), or titanium *tert*-ethoxide (TiEt, 33–35% Ti, Acros Organics) was injected into a double-necked flask (herein referred to as the bubbler) with a typical volume of 6 ml. The bubbler was then heated to the designated temperature using an isomantle, which resulted in the generation of precursor vapours. Meanwhile, the CVD reactor was heated with a cartridge heater (Watlow Firerod) until the deposition temperature was reached, which was maintained for at least 5 min before starting the reaction. High-purity nitrogen gas (99.99%, BOC®) was used as an inert gas to provide an oxygen-isolated environment in the CVD reactor and carrier gas for the precursor vapours. In this experiment, the CVD reactor temperatures ranged between 350 and 600 °C, bubbler temperatures ranged between 100 and 220 °C, and synthesis times varied from 1 to 27 min. It is important to emphasize that the studied ranges of various parameters for each precursor differ quite substantially. For instance, because of differences in precursor vaporisation points, the bubbler temperature for the TiO_2 coatings produced from TTIP ranged from 100–200 °C, whereas for TiBu, it ranged from 140–220 °C. Also, the synthesis time for the TTIP group ranged from 1–5 min with 1 min intervals, while for the TiBu group, it ranged from 3–27 min with 6 min intervals (in the case of TiEt can be found in Table S1†). Post APCVD synthesis, all TiO_2 coatings were annealed at 500 °C for 2 hours in air.

2.3 Sample characterisation

The crystal properties of the coatings were measured using X-ray diffraction (XRD). Patterns were obtained using a Bruker® D2 Phaser diffractometer equipped with a CuK_α source (λ = 1.5406 Å). The angular range of the collected patterns was set between $10° < 2\theta < 80°$ with a step size of 0.02° counted at 1 s per step. The crystal size of the sample was calculated using the Scherrer equation,[37] and the preferential orientation of the anatase phase (101), (200), (211), and (220) crystal planes was quantified using the Harris method,[38] where $I(hkl)_i$ denotes the observed peak intensity for the specific *hkl* plane, $I_0(hkl)_i$ represents its standard intensity, and n is the count of diffraction peaks taken into account (eqn (8)):

$$P(hkl)_i = \frac{I(hkl)_i / I_0(hkl)_i}{\left(\frac{1}{n}\right)\sum_i \left(I(hkl)_i / I_i(hkl)_i\right)} \quad (8)$$

Optical characterisation was conducted using a Shimadzu UV-2600 spectrometer, over a spectral range from 200 to 1000 nm. Comprehensive analyses, which included both absorbance and transmittance spectra, facilitated the estimation of the coating thickness and bandgap through the Swanepoel method[39] and the Tauc method,[40] respectively. The average visible light transmittance (VLT) of each sample was determined by averaging transmission data from 380 to 750 nm.[41]

High Resolution-Scanning Electron Microscopy (HR-SEM) was performed using a Zeiss Auriga FIB-SEM to determine the surface morphology and particle size of selected samples. A 10 nm chromium layer was sputtered before imaging using a Safematic® CCU-010 Sputter coater. Atomic Force Microscopy (AFM) was performed under ambient conditions with an Agilent™ 5500 and aluminium-coated silicon tips (Tap300AL-G). Samples were then analysed using Gwyddion 2.60® to determine the surface area and mean square roughness.[42]

Transient Absorbance Spectroscopy (TAS) was employed to measure the population and lifetime of photogenerated charge carriers in the TiO_2 coatings.[43,44] A Nd:YAG laser (355 nm, 6 ns pulse width, OPOTEK Opolette 355 II) served as the pump light, generating 355 nm UV light from the third harmonic (~2.54 mJ cm^{-2} per pulse) and a 100 W Bentham IL1 quartz halogen lamp was used as the probe light, positioned in front of the sample with a long pass filter (λ > 400 nm) and a monochromator (600 nm). A Si PIN photodiode (Hamamatsu S3071) recorded the change in transmitted light after each UV laser excitation cycle (0.667 Hz), and each TAS trace was the result of averaging 100 scans. Data at times faster than 3.6 ms were recorded with an oscilloscope (Tektronix DPO3012) after passing through an amplifier box (Costronics), whereas data slower than 3.6 ms were recorded on a National Instrument DAQ card (NI USB-6251).

2.4 Photocatalytic NO_x activity test

The photocatalytic NO_x activity of each TiO_2 coating was tested according to ISO 22197-1:2016, with a slight modification.[45] In detail, a 2 × 15 W UVA lamp was utilized as the illumination

light source, and the distance from the light source to the sample was maintained to ensure that a light intensity of 1.0 mW cm^{-2} illuminated the sample surface. The sample was placed in a gas-tight chamber topped with an acrylic lid, with an illustration of the gas flow over the sample shown in Fig. S2(b).†

The gas flow rate inside the chamber was set to 1.0 L min^{-1} by adjusting the ratio of nitric oxide (NO, 99.99%, BOC®) and air using mass flow controllers (Bronkhorst, EL-FLOW Select). The NO concentration was maintained at ~3.0 ppm at a relative humidity of ~50%. At the start of each reaction, samples were first exposed to the NO gas stream in the dark for 10 min. Subsequently, the UVA light source was turned on, and the light test was run for 30 min. Following this, the UVA light was turned off and the sample was exposed to another 10 min of the NO gas stream in the dark before being removed from the chamber. The NO and NO_2 levels were measured continuously during the reaction using a chemiluminescence NO_x analyzer (Serinus 40, Ecotech®). The degree of photocatalytic NO/NO_x conversion and propensity to form NO_2 (*i.e.* NO_2 selectivity) were calculated (eqn (9)–(11)):

$$NO_{conversion} = \frac{[NO]_{in} - [NO]_{out}}{[NO]_{in}} \times 100\% \quad (9)$$

$$NO_{x\ conversion} = \frac{[NO_x]_{in} - [NO_x]_{out}}{[NO_x]_{in}} \times 100\% \quad (10)$$

$$NO_{2\ selectivity} = \frac{[NO_2]_{out}}{[NO]_{in} - [NO]_{out}} \times 100\% \quad (11)$$

in which [*X*] represents the concentration of the gas '*X*' in ppm, in and out in subscripts mean gas concentration measured during the dark period and light period.

2.5 ML strategies and modelling

The running environment for the machine learning code was facilitated through the Anaconda® platform integrated with Python 3.11. Machine learning algorithms were executed through the Scikit Learn package 1.3.2.[46]

In this study, to achieve better prediction results, we compared six different ML strategies on the experimental dataset. The initial three strategies are:

2.5.1 Parameter oriented prediction. Only the synthetic parameters were used to predict the corresponding photocatalytic NO and NO_x activity.

2.5.2 Property oriented prediction. Only the measured physicochemical properties of the coatings were used to predict the corresponding photocatalytic NO and NO_x activity.

2.5.3 All-feature oriented prediction. Both the synthetic parameters and measured physicochemical properties of the coatings were used to predict the photocatalytic activity.

Two novel approaches (strategies 4 and 5) were introduced herein. The advantage of these two strategies is that they can predict the photocatalytic performance only through synthesis parameters without retesting the physicochemical properties for simulated data, while also being able to output the importance of the physicochemical properties simultaneously. The detailed description of them is as follows:

2.5.4 Property-prior prediction. This strategy includes a 3-step workflow. In the first step, a series of models are trained to individually predict each physicochemical property based on the synthetic parameters. In the second step, a model is trained to predict the photocatalytic activity based on the measured physicochemical properties. Finally, the model is applied by first predicting the physicochemical properties and then using these values to predict the photocatalytic activity. This approach is beneficial since we do not have full coverage of all physicochemical properties for all materials.

2.5.5 Modified property-prior prediction. Based on property-prior prediction, this strategy also includes the synthetic parameters when predicting the photocatalytic activity in the third step.

We also compared the above strategy with another strategy:

2.5.6 High property-prior prediction. Based on property-prior prediction, this strategy uses the synthesis parameters, predicted physicochemical properties, and real physicochemical properties to predict the photocatalytic activity in the third step.

A range of ML models, including Linear Regression, Random Forest Regression, Support Vector Regression, AdaBoost Regression, and XGBoost® Regression (Version 1.7.6), were employed as the fundamental components in constructing the ML strategies. To ensure optimal performance, hyperparameters were optimized using GridSearchCV coupled with param_grids before each prediction.

In order to rigorously evaluate the prediction performance of various strategies, especially adaptable to our two-tiered prediction in strategies 4–6, we adopted Nested Cross-Validation (NCV) based on the Leave-One-Out Method.[47] The core of NCV is its dual-layer validation mechanism;[48] an outer loop segregates the preliminary data set into an external test set (for model assessment) and a training set (designated for model construction and encompasses internal cross-validation). For a detailed description of NCV construction refer to Section 3.5.1.

For every ML model trained in this project, we automatically evaluate all ML regressors listed above, each with their own hyper parameter search to obtain the optimal results. This approach was additionally followed in strategies 4–6, in which ML models for each physicochemical property are trained individually. Furthermore, due to the nature of the cross validation process, the optimal model could differ between splits of the outer cross validation loop. This leads to a wide range of model architectures employed in this project.

3 Results and discussion

APCVD was used to produce 58 unique TiO_2 coatings on glass as described in Section 2.2. The nomenclature for each sample is based on their synthesis conditions which can be found in Table S1.† For instance, 001_TTIP_350_160_3 refers to the sample designated as no. 001, where TTIP was utilized as the precursor, the CVD deposition temperature and the bubbler temperature were set at 350 °C and 160 °C, respectively, and the synthesis was conducted for 3 min.

In this section, physical characterisation was first carried out to gain a qualitative understanding of the impact each synthetic parameter had on the physicochemical properties of the samples produced. The analysis is substantiated from XRD, UV-vis, SEM, AFM, and TAS results sequentially. Additionally, an overview of the trends in photocatalytic NO_x activity in relation to the synthesis parameters is presented.

More quantitative correlations between the synthesis parameters, physicochemical properties, and photocatalytic NO/NO_x activity are later revealed through ML-assisted statistical approaches, with the predictive capability of different ML strategies compared and a validation of ML simulated data under the new metric.

3.1 Effect of CVD deposition temperature

Photographs of all 58 TiO_2 coatings are shown in Fig. S3,† with two dominant types of appearance seen. One type of sample exhibited a smooth surface, with oscillations between red and blue shades seen due to variations in coating thickness, a phenomenon often seen in coatings produced using a cold-wall reactor design.[49,50] The other type of sample, at deposition temperatures above 500 °C, was more opaque and hazy, which originated from the formation of more nanostructured and thicker films, giving the TiO_2 layer its well-known white colour. All films were generally well adhered to the glass and were not prone to detachment with handling. In some cases, these thicker coatings were removed when rinsed with water. Also, in some samples, some black/brownish colour was observed, such as in sample 023_TiEt_600_160_3. This was likely due to carbon contamination arising from the carbonisation of the Ti precursor.[51,52] Although most of this dark colour was removed during the subsequent annealing process in air at 500 °C, some residual carbonation was seen in some samples.[49]

The XRD patterns of select samples are shown in Fig. 1. XRD of all 58 samples showed that the TiO_2 coatings predominantly consisted of a pure anatase phase TiO_2 ($I4_1/amd$, $a = b = 3.784$ Å, and $c = 9.515$ Å),[53,54] except samples 005_TTIP_550_160_3 and 006_TTIP_600_160_3 that contained some rutile phase TiO_2 ($P4_2/mnm$, $a = b = 4.594$ Å, and $c = 2.959$ Å), with distinct peaks seen at $2\theta = 37°$ and 68°, corresponding to the (101) and (301) crystal planes of rutile, respectively.[53] Interestingly, the observation of the rutile phase in samples produced using TTIP may be attributed to the inherent properties of the precursor, as it may undergo a different thermal decomposition pathway that leads to the nucleation and growth of the rutile phase above 500 °C.[55] However, only the anatase phase is seen in the XRD patterns of samples fabricated using TiEt and TiBu as precursors for all deposition temperatures explored herein. The preferred orientation in the anatase phase Miller planes (101), (200), (211), and (220) (corresponding to peaks at $2\theta = 27°$, 48°, 55°, and 70°) was quantified for samples produced using TTIP (Fig. S4†), TiEt (Fig. S5†) and TiBu (Fig. S6†), with no qualitative trend seen by the eye for the deposition temperatures explored herein (350–600 °C).[56] The average crystal size of the anatase phase was also quantified, and again, for the deposition temperatures explored, did not significantly differ, ranging from ~20 to 30 nm in size.

UV-visible spectroscopy was employed to assess the optical properties of the coatings (Table 1). Low light absorption within the ultraviolet region to near-infrared region (380 nm to 1000 nm) was observed in most samples, with a sharp increase in the ultraviolet region due to ultra-wide bandgap excitation of the TiO_2 coating. The indirect bandgap of most samples was in the region of 3.2 eV; consistent with the literature for anatase TiO_2.[57] There was a trend for the bandgap to marginally decrease with an increase in deposition temperature. Between deposition temperatures of 350 and 500 °C, the VLT of samples was high (~70 to 80%), whereas a significant drop in VLT was observed when the deposition temperature increased to above 500 °C (~60 to 15%). This decrease in VLT is primarily linked to the coexistence of rutile and anatase phases at high deposition temperatures when TTIP is used as the precursor, forming a more powdery, nanostructured coating.[58] The decrease in VLT with TiEt and TiBu might be attributed to the larger amount of carbon contamination compared with TTIP. The presence of

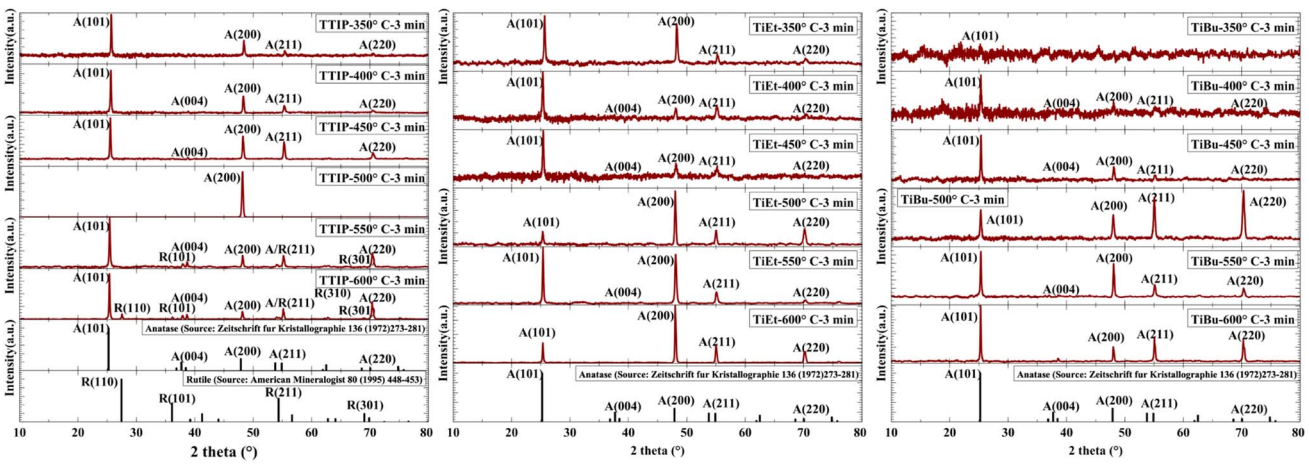

Fig. 1 XRD patterns illustrating the changes in the crystal phase, crystallinity and preferred orientation of select samples with changes in the deposition temperature and Ti precursor.

Table 1 Changes in the sample bandgap, VLT, and film thickness for TiO_2 coatings produced at a fixed bubbler temperature of 160 °C and synthesis time of 3 min, but different deposition temperatures

Experimental synthesis conditions, bubbler temperature: 160 °C, synthesis time: 3 min	Measured optical properties				
Precursor selection	Deposition temperature (°C)	Indirect b andgap (eV)	Visible light transmittance	Average thickness (nm)	Thickness error (nm)
TTIP	350	3.34	79.03	166	6.7
TTIP	400	3.42	68.6	417	5.7
TTIP	450	3.05	56.01	—	—
TTIP	500	3.11	61.43	—	—
TTIP	550	2.97	30.17	—	—
TTIP	600	2.88	18.51	—	—
TiEt	350	3.32	82.32	293	19
TiEt	400	3.29	80.24	340	7.4
TiEt	450	3.36	81.48	162	14.1
TiEt	500	3.27	71.09	712	7.9
TiEt	550	2.97	72.16	757	14
TiEt	600	3.1	47.46	1740	10
TiBu	350	—	92.57	—	—
TiBu	400	3.29	81.59	157	19
TiBu	450	3.28	84.75	212	5.4
TiBu	500	3.19	73.31	944	4.8
TiBu	550	3.08	62.45	1040	10
TiBu	600	2.95	15.08	—	—

carbon particles, which can not only increase light absorption in the visible but, depending on their size and distribution, can also introduce scattering effects within the TiO_2 film, has been discussed previously.[59,60] For less nanostructured coatings, film thickness could be determined using the Swanepoel method.[39] For deposition temperatures below 500 °C, the majority of TiO_2 coatings were between 100 and 300 nm in thickness; however, above 500 °C, film thickness was significantly higher, reaching over 1000 nm at higher deposition temperatures. A graphic plot summarising these trends can be found in Fig. S7.†

The surface topography of samples was investigated with SEM and AFM. The SEM images of select samples are shown in Fig. 2. We can see that as the temperature was increased for both the TTIP and TiEt samples, the surface structures changed from more rounded and compact particles ~100 nm in diameter seen at 450 to 500 °C, to more oblong and less compact particles ~200 nm in diameter seen at 600 °C. A noteworthy increase in Root Mean Square Roughness (R_q roughness) was observed at deposition temperatures of 550 °C and above, while the Sample Surface Area (SSA) was found to exhibit minimal

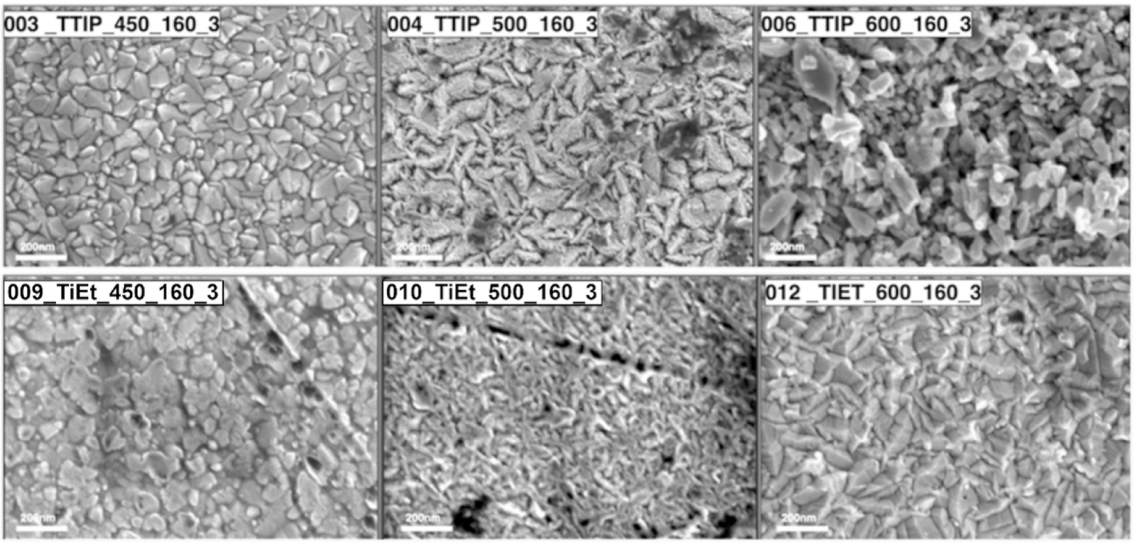

Fig. 2 SEM images illustrating the morphologies of select samples with changes in the deposition temperature and Ti precursor.

fluctuation across the range of deposition temperatures explored (see Fig. S8†). Interestingly, variations in R_q roughness were influenced significantly by the choice of the precursor. Specifically, when TTIP was employed, a marked increase in R_q roughness was consistently seen in comparison to TiEt and TiBu.[58]

TAS measurements were conducted at a probe wavelength of 650 nm, utilizing 355 nm laser excitation, spanning the microsecond to second timescale (Table S3†). Previous work has established that the transient absorption at 650 nm in anatase and rutile TiO_2 is a composite signature of both electron and hole carriers.[43,44] The recombination kinetics in most samples herein followed a power law decay, typical of anatase TiO_2 and the thermally governed mechanism of electron trap-hopping and eventual recombination with holes. Typical mΔO.D. at 10 μs after laser excitation of ∼0.10 to ∼0.20 ms was observed alongside relaxation to half the signal seen from 10 μs after laser excitation ($t_{50\%}$) of ∼0.2 to ∼0.3 ms; these values are quite typical of anatase TiO_2 coatings grown by CVD.[43] Regardless of precursor selection, significant increases in charge carrier populations were seen at higher deposition temperatures, which we attribute to the increased harvesting of the 355 nm laser pump as film thickness increases with deposition temperature. On the other hand, the $t_{50\%}$ values did not exhibit a consistent trend with temperature. Nevertheless, some coatings grown at elevated temperatures, such as 600 °C for TTIP and 550 °C for TiBu, showed pronounced increases in $t_{50\%}$.

The influence of deposition temperature on photocatalytic NO_x activity is shown in Fig. 3. Fig. 3(a) shows that for deposition temperatures below 500 °C, all samples showed NO conversions in the range 0.3 to 2.0%, surpassing the 0.2% benchmark value seen in a commercial self-cleaning glass. However, at deposition temperatures above 500 °C, there was a pronounced increase in NO and NO_x activity, with coatings showing maximal conversions at a deposition temperature of 600 °C. Evidently, at higher growth temperatures, the coatings demonstrate higher catalytic activity. The overarching trend was for NO and NO_x conversions to be proportional, with NO_2 selectivities generally in the 50 to 80% range. However, given the low conversions seen in several samples, the NO_2 selectivities possessed high associated errors. It should be clarified that in our chart, the error bars represent an 80% confidence interval, and the error bars are relatively wider in the results for NO_2 selectivity compared to NO/NO_x conversion. This is because when calculating the error of NO_2 selectivity, one must propagate errors from both NO and NO_x conversion data, as shown in eqn (11).[61] This leads to an expansion of the NO_2 selectivity error range, but we believe this is necessary, as it provides a comprehensive and rigorous error assessment. Overall, there were some notable samples, with 012_TiEt_600_160_3 achieving an impressive NO conversion of 22.7% (and 18.0% under ISO test conditions, shown in Fig. 3(b)), whereas 014_TiEt_400_160_3 exhibited the lowest NO_2 selectivity of ∼9.2%. It should be noted that the steady-state formation of NO_2 should be avoided where possible, as this can worsen air quality given its higher toxicity compared to NO.[62] This, and other aspects, will be assessed by ML and discussed in more detail in Section 3.5.1.

3.2 Effect of synthesis time

Under deposition temperatures of 450 °C and 500 °C, the impact of synthesis time on the physicochemical properties of materials and NO_x conversion efficiency was examined for a fixed bubbler temperature of 160 °C. It was found that the physicochemical properties of the materials were affected by the synthesis time and precursor. When TTIP was utilized as the precursor, more evident changes were observed in both the

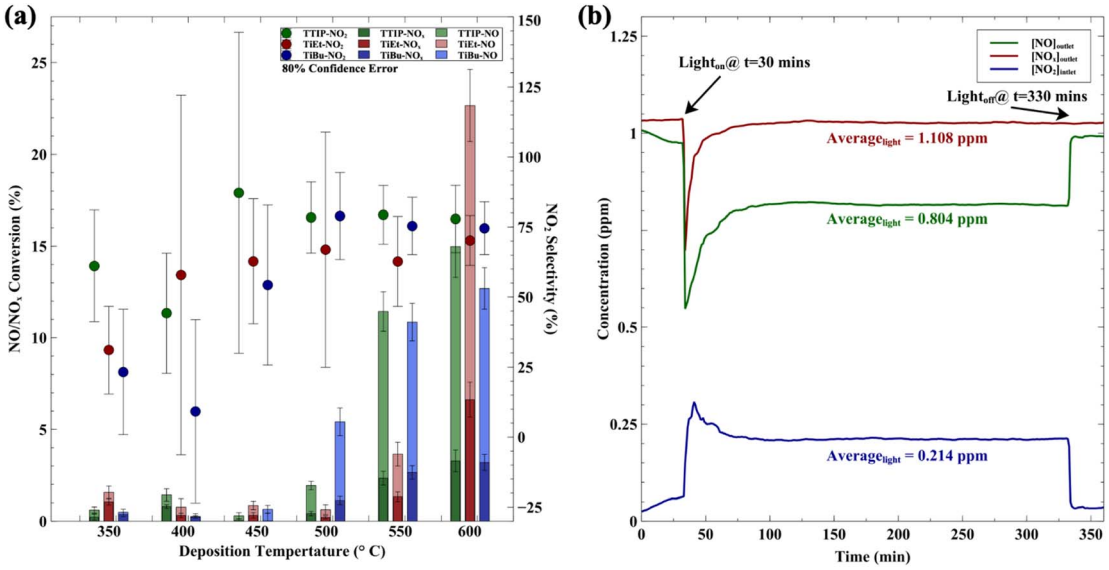

Fig. 3 (a) Photocatalytic NO/NO_x conversion (bar chart) and NO_2 selectivity (scatter chart) of samples grown with differing deposition temperature (green-TTIP, red-TiEt, and blue-TiBu, from sample 001 to sample 012). (b) Photocatalytic NO_x measurement of sample 012_TiEt_600_160_3 measured under near-ISO test conditions (red-NO_x, blue-NO_2, and green-NO).

physicochemical properties and photocatalytic NO_x conversion efficiency. However, when materials were synthesized using TiEt and TiBu as precursors, less pronounced variations in their physicochemical properties and photocatalytic efficacies were seen. Therefore, the primary focus of the subsequent discussion is on the effect of synthesis time on the material properties and photocatalytic performance when TTIP was used.

For TTIP, for a synthesis time of 1 min, a film displaying colour contours was produced, indicating the formation of a flat and dense film. However, with the extension of the synthesis time to 5 min, a more powdery coating was produced. These observations were more pronounced at higher deposition temperatures. In terms of their crystal properties, at a deposition temperature of 450 °C, a systematic decline in the 200-plane was observed as the synthesis time was increased (Fig. S9†). This was coupled with an enhancement in the 220-plane as the synthesis time was increased. At a deposition temperature of 500 °C, a strong preferred orientation in the (211) plane was lost as the synthesis time was increased, with resulting increases in the (220) plane (Fig. S10†). This shift might have been a result of the increased conversion of the material from the anatase to the rutile phase at 500 °C. The production of the composite phase resulted in the formation of a more powdery coating. Besides, as the synthesis time was increased at 500 °C, the average crystal size increased from ~20 nm at a 1 min synthesis time to ~30 nm at a 5 min synthesis time. Interestingly, this effect was not seen for TiEt (Fig. S11†) and TiBu (Fig. S12 and S13†) with regard to changes in average crystal size due to increases in synthesis time.

The optical properties of the samples were also examined, with no significant bandgap changes seen with increases in synthesis time for TTIP (Fig. S14†), TiEt (Fig. S15†) and TiBu (Fig. S16†). Nevertheless, variations in the thickness trends of the samples were dictated by the choice of precursor and deposition temperature. Specifically, with the use of TiEt as the precursor at a deposition temperature of 500 °C, a gradual increase in product thickness was observed with extended synthesis time. Similarly, with TiBu as the precursor at a deposition temperature of 450 °C, a moderate increase in coating thickness from ~200 to 650 nm was seen as the synthesis time was increased from 3 to 27 min. At 500 °C, the thickness increased between ~400 and 900 nm. The growth rate of sample thickness, when either TiEt or TiBu was utilized as the precursor, remained similar, with an approximate increase in film thickness of 300 nm per 12 min of synthesis. In contrast, a substantially faster reaction rate was seen when TTIP was utilized, with nearly a 1000 nm increase in film thickness seen when the synthesis time was increase from 1 to 2 min, followed by more moderate increases in the growth rate.

Example SEM images are shown for samples produced using TTIP and TiEt, where increases in synthesis time increased the uniformity and density of the crystals formed (Fig. S17†). Using AFM, the effect of synthesis time on the R_q roughness and SSA of coatings was assessed for TTIP (Fig. S18†), TiEt (Fig. S19†) and TiBu (Fig. S20†). For TiEt and TiBu, the SSA remained approximately constant for all synthesis times and deposition temperatures examined; however for TTIP, the SSA increased sharply at a synthesis time of 5 min at a deposition temperature of 500 °C from ~27 to ~35 μm^2 per 25 μm^2 geometric area. This was coupled with a substantial increase in R_q roughness from ~20 to ~140 nm. For TiEt, the R_q roughness did not change significantly with synthesis time, remaining at around 10 to 20 nm; however for TiBu, there was a tendency for R_q roughness to increase at a deposition temperature of 500 °C from ~10 to 40 nm when the synthesis time was increased from 3 to 27 min.

The impact of synthesis time on the charge carrier population and lifetime was found to be significant but was also controlled by the precursor used. When TTIP was chosen, a pronounced increase to both charge carrier population and lifetime was observed at the longest synthesis time of 5 min, regardless of the deposition temperature. In contrast, for samples synthesized using TiEt and TiBu as precursors, a more steady increase in both the charge population and lifetime was exhibited with increases in synthesis time, instead of the abrupt jump observed in the TTIP group. The charge population and lifetimes appeared to plateau at a synthesis time of ~9 min for TiEt and ~15 min for TiBu. The numerical details of these results can be viewed in Table S3†.

The effects of synthesis time on photocatalytic NO_x activity is shown in Fig. 4 for a fixed bubbler temperature of 160 °C. Broadly speaking, most samples showed NO conversion levels between 0.5 and 2%. For TTIP, consistently low NO_x conversion rates were seen for all synthesis times at a deposition temperature of 450 °C. However, at a deposition temperature of 500 °C, an increased synthesis time was seen to be highly beneficial to photocatalytic activity, reaching NO conversion rates of ~5.5% at a synthesis time of 5 min. For samples made using TiEt at a bubbler temperature of 160 °C and deposition temperature of 500 °C, there was seemingly no benefit to photocatalytic activity

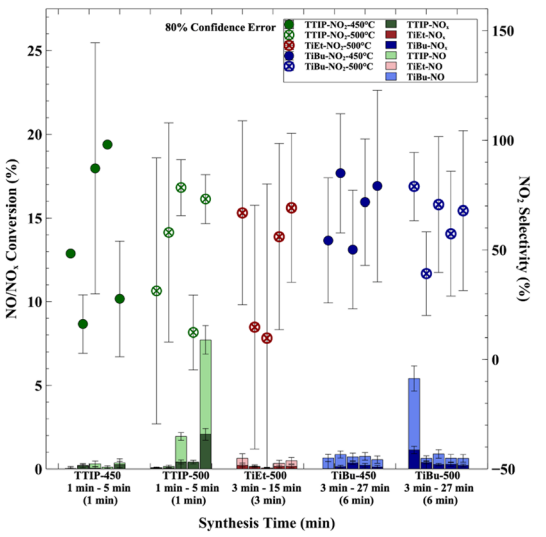

Fig. 4 Photocatalytic NO/NO_x conversion (bar chart) and NO_2 selectivity (scatter chart) of samples grown with varying synthesis time for a fixed bubbler temperature of 160 °C (green-TTIP, red-TiEt, and blue-TiBu); the range of times specified represents the range of synthesis times studied from left to right in the bar chart, with times in brackets beneath representing the time intervals between each bar.

in increasing the synthesis time. However, at a deposition temperature of 500 °C, an increased synthesis time was found to be clearly detrimental to photocatalytic activity for samples made using TiBu. The reasons for this trend are unclear, with a possible explanation being an increased tendency to form carbon deposits within the TiO_2 film, which are detrimental to photocatalytic activity at longer synthesis times using this precursor. Specifically, samples 037_TiEt_500_160_9 and 049_TiBu_500_160_9 exhibited notably low NO_2 selectivity, where more generally, an increase in NO_2 selectivity was observed when TiEt and TiBu were used as precursors, whereas a decrease was noted when TTIP was used.

3.3 Effect of bubbler temperature

The precursor bubbler temperature in the CVD process controls the amount of precursor that is transferred into the reactor during the deposition, which can be calculated from the vapour pressure curve of each precursor.[63–65] In this work, bubbler temperatures were chosen that would result in a range of film thicknesses. Generally speaking, at lower bubbler temperatures, the coatings grown tended to be thinner and more compact; at moderate bubbler temperatures more nanostructured and hazy depositions were observed; at high bubbler temperatures (approaching the boiling point of the precursor) a much more cracked and powdery coating was obtained with a greater amount of carbon contamination (*e.g.* sample 051_TiBu_500_220_3 in Fig. S3†).

With regard to the physicochemical properties of the coatings, the crystal and optical properties were not substantially impacted by the changes in bubbler temperatures examined herein. For TTIP, at a deposition temperature of 450 °C, there was no significant change in the average crystal size with an increase in bubbler temperature from 100 to 180 °C (Fig. S21†). However, there is a small notable tendency for growth in the (200) plane to decrease with bubbler temperature and for growth in the (220) plane to increase with bubbler temperature. For TTIP, at a deposition temperature of 500 °C, the average crystal size decreased marginally from ~27 to ~20 nm with an increase in bubbler temperature from 100 to 180 °C (Fig. S22†). Similar to TTIP at a deposition temperature of 450 °C, TiEt showed the same trend for the (200) plane to decrease with bubbler temperature and for the (220) plane to increase with bubbler temperature (Fig. S23†). For TiBu at a deposition temperature of 450 °C, there was a broad trend for average crystal size to decrease from ~27 to ~13 nm with an increase in bubbler temperature from 140 to 220 °C (Fig. S24†). However, for TiBu at a deposition temperature of 500 °C, there was no significant effect of changing the bubbler temperature on the crystal properties observed (Fig. S25†). With regard to the optical properties of the coatings, there was no significant change seen in either the indirect allowed optical bandgap or the VLT of the coating with changes in bubbler temperature for TTIP (Fig. S26†), TiET (Fig. S27†) or TiBu (Fig. S28†).

However, as we discussed above, the correlation between the coating thickness and bubbler temperature is more visible by characterisation, which can be viewed in Table S2†. As a result, in terms of TiEt, a steady rise in coating thickness from ~200 to ~700 nm at 3 min synthesis time is caused by an increase in the bubbler temperature from 120 to 200 °C. This indicates that a larger amount of the precursor is successfully transferred into the CVD reactor and deposited on the glass. However, for TiBu, a decrease in material thickness was seen with an increase in the bubbler temperature from 140 to 220 °C. This emphasizes that the growth of the TiO_2 coating can be hindered by the production of carbon contamination in the sample, which was an issue for TiBu at higher bubbler temperatures.

SEM imaging was used to investigate the surface morphology of the samples synthesized at temperatures of 450 °C and 500 °C using TiBu, as shown in Fig. S29.† The sample 052_TiBu_450_220_3 exhibited almost no recognizable morphology under high resolution, which may be attributed to the formation of a highly smooth and thin coating on the glass substrate. In contrast, a rice-like morphology, was shown by samples synthesized at 500 °C, particularly when the bubbler temperature was 220 °C, with clearer boundaries between particles observed, alongside an increase in particle size.

In terms of the charge carrier kinetics, an increase in charge carrier populations and lifetimes was typically seen with increases in bubbler temperature. When TTIP and TiEt were used, these values seemingly reached a plateau at particular bubbler temperatures. In contrast, higher values at higher bubbler temperatures were obtained when TiBu was used as the precursor. An impressive 0.105 m ΔO.D. and $t_{50\%}$ of 71.1 ms were seen when the bubbler temperature was set at 220 °C with TiBu for a deposition temperature of 450 °C and synthesis time of 3 minutes. A high charge carrier lifetime of 23.3 ms was observed in sample 042_TiEt_500_120_3. The numerical details are summarised in Table S3†. AFM analysis showed that there was no clear correlation between the R_q roughness or SSA with changes in bubbler temperature for depositions at 450 and 500 °C using TTIP (Fig. S30†), TiEt (Fig. S31†) or TiBu (Fig. S32†). However, it should be noted that there was greater variation in R_q roughness seen in the samples made using TiBu.

The effect of bubbler temperature (100 to 220 °C) for deposition temperatures between 450 and 500 °C on the photocatalytic NO_x activity is shown in Fig. 5. For TTIP and TiEt, there was no clear correlation between bubbler temperature and photocatalytic activity. However, for TiBu at a deposition temperature of 450 °C, a higher bubbler temperature was beneficial to activity, and at 500 °C, a higher bubbler temperature was detrimental to activity.

3.4 Effect of precursor selection

The effect of precursor selection is assessed in this section by averaging the data generated from all coatings made by each precursor. Their physicochemical and photocatalytic properties are summarised in Table 2, with a comparison with commercial self-cleaning glass and a TiO_2-based commercial product, Cristal ACTiV™ PC-S7.

With regard to film thickness, coatings produced using TTIP were thicker (~890 nm) than coatings produced using TiEt (~606 nm) or TiBu (~684 nm). However, samples made from

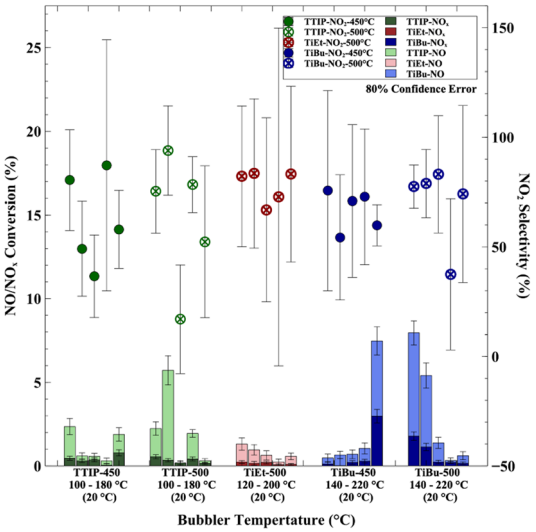

Fig. 5 Photocatalytic NO/NO_x conversion (bar chart) and NO_2 selectivity (scatter chart) of samples grown at differing bubbler temperatures for a fixed synthesis time of 3 min (green-TTIP, red-TiEt, and blue-TiBu); the range of temperatures specified represent the range of bubbler temperatures studied from left to right in the bar chart, with temperatures in brackets representing the temperature intervals between each bar.

TiEt had the highest VLT at ~74.1%, whereas those produced from TTIP had the lowest VLT of ~59.7%. The thickness of typical commercial self-cleaning glass is significantly lower at ~12 nm.[66] It should be noted that commercial self-cleaning glass is optimized to maintain high VLT, necessitating a lower thickness. While this design choice clearly benefits optical transparency, it may not benefit photocatalytic performance.[29] Even so, the thickness of our product is still far lower than that of other TiO_2-based photocatalytic coatings for non-glazing applications, which possess a usual thickness of larger than 1 μm.

The average crystal size and preferred orientation of samples for each precursor are shown in Fig. 6(a). For TTIP, on average, coatings possess a larger average crystal size of ~27 nm compared to those produced using TiEt (~22.3 nm) and TiBu (~23.5 nm). On average, the precursors used herein produced coatings that possessed mild average crystals with a size between those of a commercial self-cleaning standard (~18 nm)[66,68] and painted P25 TiO_2(~25 nm).[24] On average, in our work, TTIP coatings had a higher preference to orient in the (200) plane, contrasting with TiBu and TiEt, which showed a higher preference to orient in the (220) plane. The R_q roughness and SSA showed that samples derived from TTIP had an average roughness of ~32.7 nm, which was notably higher than those from TiBu (~17.8 nm) and TiEt (~15.2 nm) Fig. 6(b)). Changes in the SSA were similar, with an average of ~27.5 μm^2 seen in TTIP, ~26.5 μm^2 seen in TiBu, and ~26.0 μm^2 seen in TiEt per geometric area of 25 μm^2.

TAS analysis showed that samples produced using TTIP and TiEt, on average, exhibited the highest average charge carrier populations at 10 us (0.43 and 0.44 mΔO.D., respectively), which was significantly higher than those produced using TiBu (0.20 mΔO.D.). However, the average $t_{50\%}$ of samples produced from TiBu (4 ms) was higher than those from TTIP and TiEt (1.02 and 2.05 ms, respectively), suggesting that a higher charge population does not result in a higher charge carrier lifetime, and indicates that the photogenerated charges live longer in films produced using TiBu. We postulate that when different precursors are used, it results in varying levels of defect sites in

Table 2 Averaged physicochemical properties and photocatalytic NO_x performance for each precursor seen across the 58 samples produced herein (TTIP = 22 samples; TiEt = 14 samples; TiBu = 22 samples), and compared properties values with those of commercial self-cleaning glass and TiO_2-based commercial products

Properties and performance		TTIP	TiBu	TiEt	Commercial self-cleaning glass[66]	Cristal ACTiV™ PC-S7 [24,67]
Crystal properties	Crystal size (nm)	26.9	23.5	22.3	18.0	25
	(101) Phase orientation	0.40	0.34	0.42	—	80% anatase and 20% rutile
	(200) Phase orientation	1.39	0.85	0.99	—	
	(211) Phase orientation	0.65	0.79	0.97	—	
	(220) Phase orientation	1.12	1.78	1.41	—	
Optical properties	Bandgap (eV)	3.12	3.2	3.21	—	3.16
	VLT (%)	59.7	69.5	74.1	77.0	—
	Average thickness (nm)	890	606	684	12.0	100 (μm)
Surface properties	R_q roughness (nm)	32.7	17.8	15.2	0.27	—
	Mean roughness (nm)	25.4	13.7	11.6	0.18	—
	Sample surface area (μm^2 per geometric 25 μm^2)	27.5	26.5	26.0	—	50
Charge kinetics	Population @ 10 s (mΔO.D.)	0.43	0.20	0.44	0.0085	—
	$t_{50\%}$ from 10 μs (ms)	1.02	4.00	2.05	0.21	—
Photocatalytic performance	NO conversion (%)	2.17	2.54	2.45	0.27	46.0
	NO_x conversion (%)	0.59	0.70	0.78	0.18	34.8
	NO_2 selectivity (%)	60.2	63.1	58.8	34.8	23.0
Cost for per 1 L feedstock in GBP (£)		98.30	115	314	227.1	639 (1 kg)

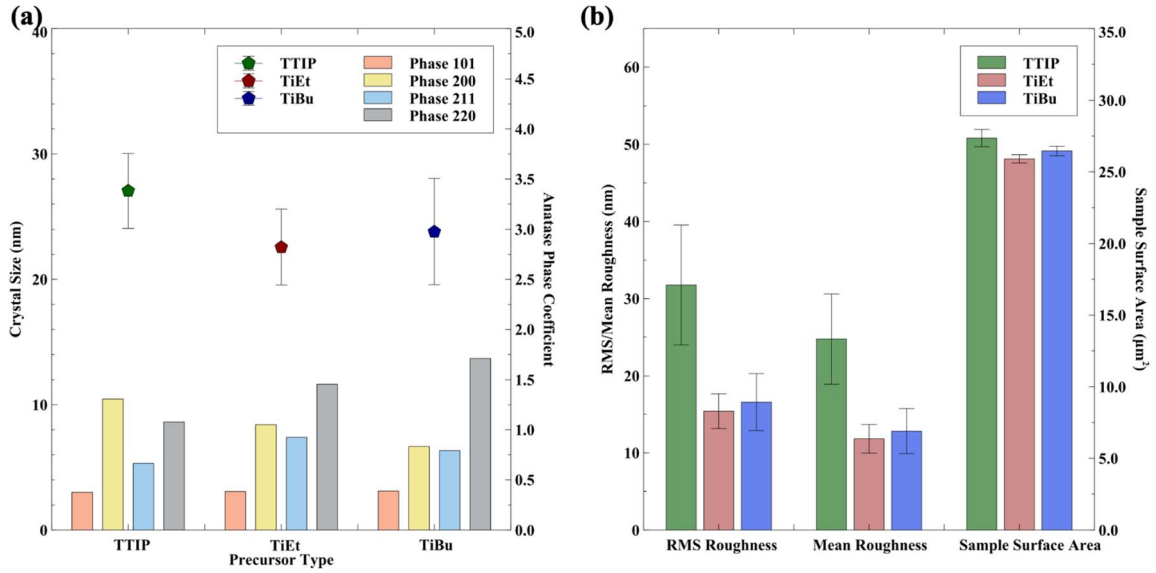

Fig. 6 The effect of the precursor type on (a) average crystal properties and (b) average surface properties (R_q roughness and SSA) seen across the 58 samples produced herein (TTIP = 22 samples; TiEt = 14 samples; TiBu = 22 samples). Error bars represent 80% confidence intervals.

the products due to their varying decomposition pathways. It is well known that defects have a strong effect on the lifetime of photogenerated charge carriers.[69]

In terms of the average photocatalytic NO_x conversion, samples employing TiEt as the precursor exhibited the highest average NO_x conversion rate of 0.78%, whereas samples made using TTIP had the lowest average NO_x conversion of 0.59% (shown in Fig. 7). In comparison, regardless of the precursor selection, the performance of our products in both NO conversion and NO_x conversion surpassed that of commercial self-cleaning glass measured under the same conditions, with a NO_x conversion rate of only 0.18%. On the other hand, the average performance of our materials is notably lower than that of other TiO_2-based materials used for NO_x removal, such as Cristal ACTiV™ PC-S7.[67] TiO_2 coatings produced using APCVD differ from photocatalytic materials that incorporate TiO_2 nanopowder powder; they have often a lower surface area and therefore less active, but can maintain high transparency and can be significantly more durable to abrasion lending themselves to applications for self-cleaning windows.

Nevertheless, while TiEt has a higher average NO/NO_x conversion efficiency, it might not be a favourable choice when simultaneously considering production costs. The cost of TiEt feedstock is nearly 1.5 times than that of those used in the current production of commercial self-cleaning glass, which employs ethyl acetate and $TiCl_4$ as raw materials.[55,66] Conversely, using TTIP and TiBu could effectively reduce production costs while maintaining higher photocatalytic activity.

Lastly, it is important to acknowledge that, under a pure NO stream, our samples exhibit a higher NO_2 selectivity (~60%) compared to some commercial products (20–30%). We have calculated the $DeNO_x$ index in Table S4 in the ESI† to highlight this issue, where a negative $DeNO_x$ index value expresses increase in total toxicity in photocatalytic oxidation of NO. However, it should be noted that under real-world test conditions, both NO and NO_2 would be present, and therefore, an increased $DeNO_x$ index value would likely be seen for our coatings.

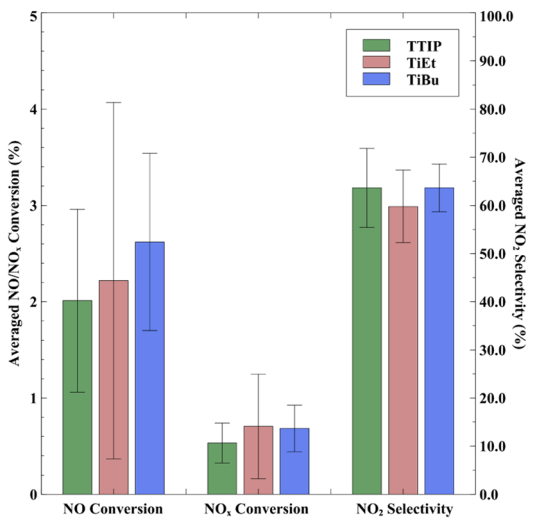

Fig. 7 The effect of the precursor type on average photocatalytic NO_x activity seen across the 58 samples produced herein (green-TTIP = 22 samples; red-TiEt = 14 samples; blue-TiBu = 22 samples). Error bars represent 80% confidence intervals.

3.5 ML-assisted insights into photocatalytic NO_x activity prediction

We now investigate the potential for ML methods to learn how the synthetic and measured properties are correlated. The full experimental data set is presented in Table S5†. To avoid confusion, the abbreviations used in Table S5† and the

following context are emphasized here. Significantly, "R_q" represents "Root Mean Square Roughness", "SSA" represents "Sample Surface Area", "Charpop" represents "Photogenerated Charge Population", and "Charlife" represents "Photogenerated Charge Lifetime". In addition, including crystal size (crystal size), different crystal phase coefficients (101 phase, 200 phase, 211 phase, and 220 phase), band gaps (Bandgap) and visible light transmittance (VLT) are also evaluated in ML modelling (The Pearson correlation coefficients between each pair of variables were calculated and can be referred in Fig. S33†).

The data from sample 013 and sample 014 were not placed in the data set. This is because their charge carrier behaviour did not provide measurable values under the conditions applied. A total of 56 samples were therefore applied in our ML process.

3.5.1 Optimal strategies for photocatalytic NO/NO_x conversion prediction. In machine learning, the division of the dataset significantly constrains the prediction of model performance.[48,70] Here, we propose a more rigorous method. A flowchart in Fig. 8 illustrates our process for determining the best strategy for predicting photocatalytic NO_x performance from the material synthetic parameters and properties from our data set. This method was inspired from Nested Cross Validation (NCV), which can avoid the risk of data leakage using a two-tiered prediction method, applied in strategies 4–6.[70]

In detail, a sample splitting method based on Leave-One-Out Cross Validation (LOOCV) is adopted. This involved defining a sampling function that traverses the data set, taking one sample from the entire data and all other samples as training data. In this way, each sample will serve as the only test data in the test set in all 56 test cycles, and these data only appear in the test and do not participate in the decision of any best model in the ML training. The accuracy of the strategy over a period is obtained by comparing the mean square error (MSE) between the actual values of the test data and the predicted values of it. Finally, the average MSE obtained during these 56 cycles is used to calculate the final score of the evaluation strategy. In each cycle, various primary regression methods, including linear regression, support vector regression, random forest regression, Adaboost regression, and XGboost regression were, successively trained and evaluated using the divided training set. The method demonstrating the highest predictive accuracy was selected to assess the following photocatalytic NO_x activity prediction capability among various strategies using the test set. Again, it is noteworthy that we do not designate which primary ML method to use in each data split; however, the selections for eventual prediction are automatic and will differ in each group.

A comparison of all strategies (discussed in Section 2.5) for photocatalytic NO/NO_x conversion predictions and NO_2 is shown in Fig. 8. The average MSEs from 56 cycles between predicted and actual values for different strategies are shown on the corresponding *y*-axes, representing the performance of strategies in different data-splits. If a strategy exhibits a more concentrated distribution around a lower MSE value, it demonstrates a more stable and superior predictive accuracy. The colourmap denotes the count of MSEs gained from these strategy turns, which fall into a specific interval (with all MSE distributions split into 25 intervals). As more MSE values lie within an interval, the colour shifts more towards yellow, emphasizing the relative stability of the strategy across various data splitting and sampling.

The strategy with the most favourable accuracy for photocatalytic NO conversion prediction was identified as "modified property-prior strategy" (average MSE = 8.63), followed closely by "parameter orientated prediction" (average MSE = 9.46) and "all-feature orientated prediction" (average MSE = 11.71). On the other hand, relative to other strategies, the "modified property-prior strategy" exhibits a narrower MSE distribution. This shows that the "modified property-prior strategy" has both stronger predictive capability and higher tolerance for different data splitting. In other words, it indicates a higher reliability for the data simulation when employing this strategy. In terms of photocatalytic NO_x conversion prediction, "parameter orientated prediction" is seen to be the best strategy (average MSE = 0.68), followed closely by "property-prior prediction" (average MSE = 0.72) and "modified property-prior prediction" (average MSE = 0.73), and they exhibit an obvious narrower MSE distribution than the other three strategies, highlighting the robustness of their predictions. It's worth noting that since the data are not normalized during modelling, the average MSE score for predicting photocatalytic NO and NO_x will differ due to a wider range of values seen in photocatalytic NO conversion compared with photocatalytic NO_x conversion. It does not mean that using this strategy to predict photocatalytic NO_x conversion is more suitable compared with NO prediction, and therefore, the performance of each strategy for predicting photocatalytic NO and NO_x should be evaluated respectively.

All strategies show more random MSE distributions and higher MSEs in the prediction of NO_2 selectivity over 56 cycles. More or less, the "modified property-prior strategy" and "property-prior strategy" perform the best, with the lowest scores of 680 and 698, respectively. It is surprising that the two-tiered models based on predicted properties show better performance in predicting different photocatalytic targets, and we also noticed that strategies that include real properties in the target prediction process (*i.e.* strategies 2,3, and 6) always get lower MSEs and broader MSE distributions. A possible reason is that the predicted properties smooth the noise in the experimental measurements, so the relationship between these attributes and targets can be learned more easily during the ML prediction process.

In addition, when the model predicts photocatalytic performance, the data points with higher true corresponding target values generally obtain a higher prediction error. This shows that ML predictions are more likely to underestimate the photocatalytic conversion performance of the material. This may also be caused by limitations in our data. For example, the data points with excellent performance (*i.e.*, high photocatalytic conversion performance) are relatively sparsely distributed. Therefore, when these high-performance data points are selected as the test set, the model is faced with a more scarce training set of high-performance examples, and high performance samples are omitted in some groups. This results in the model being unable to effectively learn the actual data

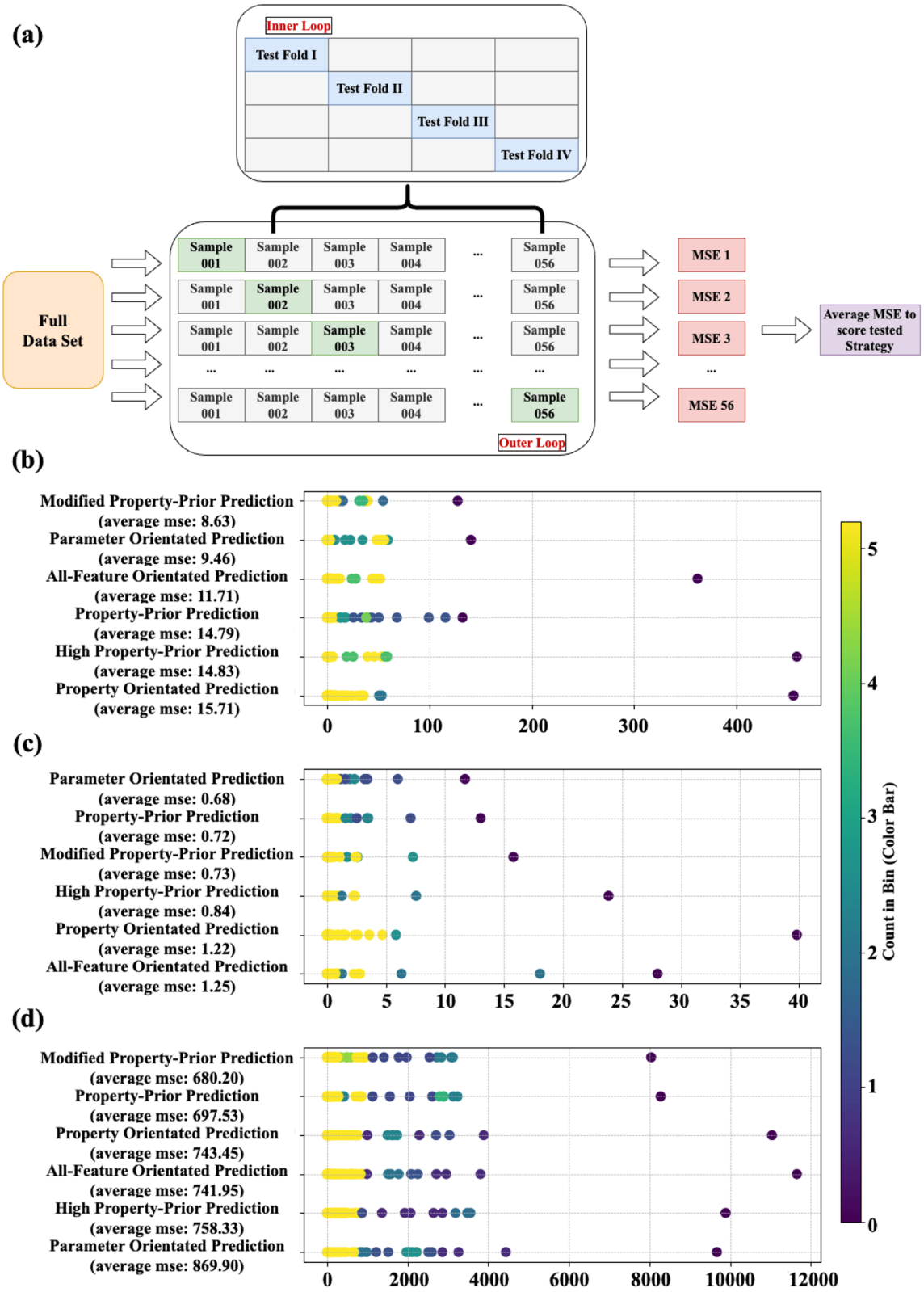

Fig. 8 (a) Evaluation of the ML strategy based on LOOCV and NCV, and visualized performance of Mean Squared Error (MSE) in predicting (b) photocatalytic NO conversion, (c) photocatalytic NO_x conversion and (d) photocatalytic NO_2 selectivity in 56 NCV cycles for each ML strategy, where colours represent the number of times the MSE falls within this range.

distribution during training; therefore, the model's insufficient ability to generalise these data points during the learning process results in an underestimation of the material's photocatalytic performance predictions.

3.5.2 Predictive performance based on optimal strategies. Given their lowest MSEs, the "modified property-prior strategy" was used to predict NO conversion and NO_2 selectivity on the entire data set, while the "property-prior strategy" was used to predict NO_x conversion from our synthesis parameters and physicochemical data in this work. A 5-fold cross-validation is used to determine the best model in each prediction step. The results of this are summarized in Table 3.

Fig. 9(a)–(c) show the scatter plot of NO conversion, NO_x conversion and NO_2 selectivity on the predicted results against their real results, respectively. Their average MSE and R^2 scores are also indicated in the plots. The data show that the average MSE of the model for predicting NO conversion is 4.87, and the average MSE of the model for predicting NO_x conversion and NO_2 selectivity is 0.85 and 359 respectively. This means that the model's errors in predicting the three target values are $\pm$2.21, $\pm$0.92, and $\pm$18.95% respectively. In the process of predicting NO, the model's test values and actual values have a high degree of agreement (R^2 is $\sim$0.75), whereas, in predicting NO_x conversion and NO_2 selectivity, the model's agreements are worse (R^2 is approximately 0.36 and 0.29, respectively). As mentioned above, the model underestimates data points with high performance to some extent and tends to concentrate NO_2 selectivity between 40 and 80%. We recognize that the R^2 values were lower for these functional properties, which is mainly caused by the inherent uncertainty within the dataset itself. The relatively lower R^2 values reflect the model's response to the complexity of the data, rather than solely indicating a deficiency in the performance of the model. Of course, some physicochemical properties that strongly govern these functional properties may not have been considered in the dataset, such as the charge carrier mobility, *etc*. However, it should be noted that our ML predictions have to some extent reduced the randomness of the original data and made trends among the data clearer. From Fig. 9, we found that the ML model still effectively recognized whether the data point is a potential "high performance" point. This demonstrates that the ML model has successfully captured the general data trends through the measured sample properties, and this indicates that the model can be employed to primarily judge whether a product would have potential high NO_x photocatalytic oxidation performance based only on the synthesis conditions in future industrial production and experimental design, and thereby enables an efficient screening of promising material designs and avoids time-consuming "trial-and-error" approaches (see Section 3.5.3).

SHAP values (Shapley Additive ExPlanations value plots), consequently, were used to measure the contribution of each feature towards the model's prediction.[71] This provided insight into which input features had a stronger influence on photocatalytic NO and NO_x activity prediction. The SHAP plot for the NO conversion of the material is plot in Fig. 9(d) below. In the plot, a positive SHAP value indicates an enhancement in the predictive performance of the feature, while a negative SHAP value denotes a diminishment.[72] From these results, it can be concluded that sample surface roughness and charge carrier lifetime are the most influential factors that control photocatalytic NO_x conversion. However, features such as the crystal properties as well as the bandgap are seen to have minor predictive contributions also. This result coincides with our experimental observations. Moreover, the positive and negative SHAP values indicate the enhancement or weakening of the prediction performance by the feature values of the feature. Taking the SSA of the sample as an example, scatter points with higher SHAP values tend to have higher feature values (pink color), which indicates that it is easier to obtain high NO removal efficiency for samples with higher surface areas. In contrast, as for VLT, although it does not play a decisive role in the determination of NO conversion, when the SHAP value is higher, VLT exhibits lower values (blue color), which shows that

Table 3 Summary of the optimised ML models and their hyper-parameters to predict each input feature

Predicted feature	Best regression model	Optimized hyper-parameter
Crystal size	AdaBoost regressor	Learning_rate = 0.001, *n*_estimators = 100
101 phase	XGB regressor	Learning_rate = 0.1, *n*_estimators = 50, max_depth = 3
200 phase	SVR	C = 1, gamma = 1, kernel = 'rbf'
211 phase	AdaBoost regressor	Learning_rate = 0.1, n_estimators = 100
220 phase	AdaBoost regressor	Learning_rate = 1, n_estimators = 100
Bandgap	Random forest regressor	*n*_estimators = 200, min_samples_leaf = 2, min_samples_split = 10
VLT	Random forest regressor	*n*_estimators = 50, min_samples_split = 5, max_depth = 10
R_q	SVR	C = 100, gamma = 0.1, kernel = 'rbf'
SSA	XGBRegressor	Learning_rate = 0.1, *n*_estimators = 200, max_depth = 7
Charpop	XGBRegressor	Learning_rate = 0.001, *n*_estimators = 200, max_depth = 7
Charlife	SVR	C = 10, gamma = 1, kernel = 'rbf'
NO	AdaBoost regressor	Learning_rate = 0.01, *n*_estimators = 100
NO_x	SVR	C = 10, gamma = 0.001, kernel = 'rbf'
NO_2	Random forest regressor	*n*_estimators = 200, min_samples_leaf = 2, min_samples_split = 10

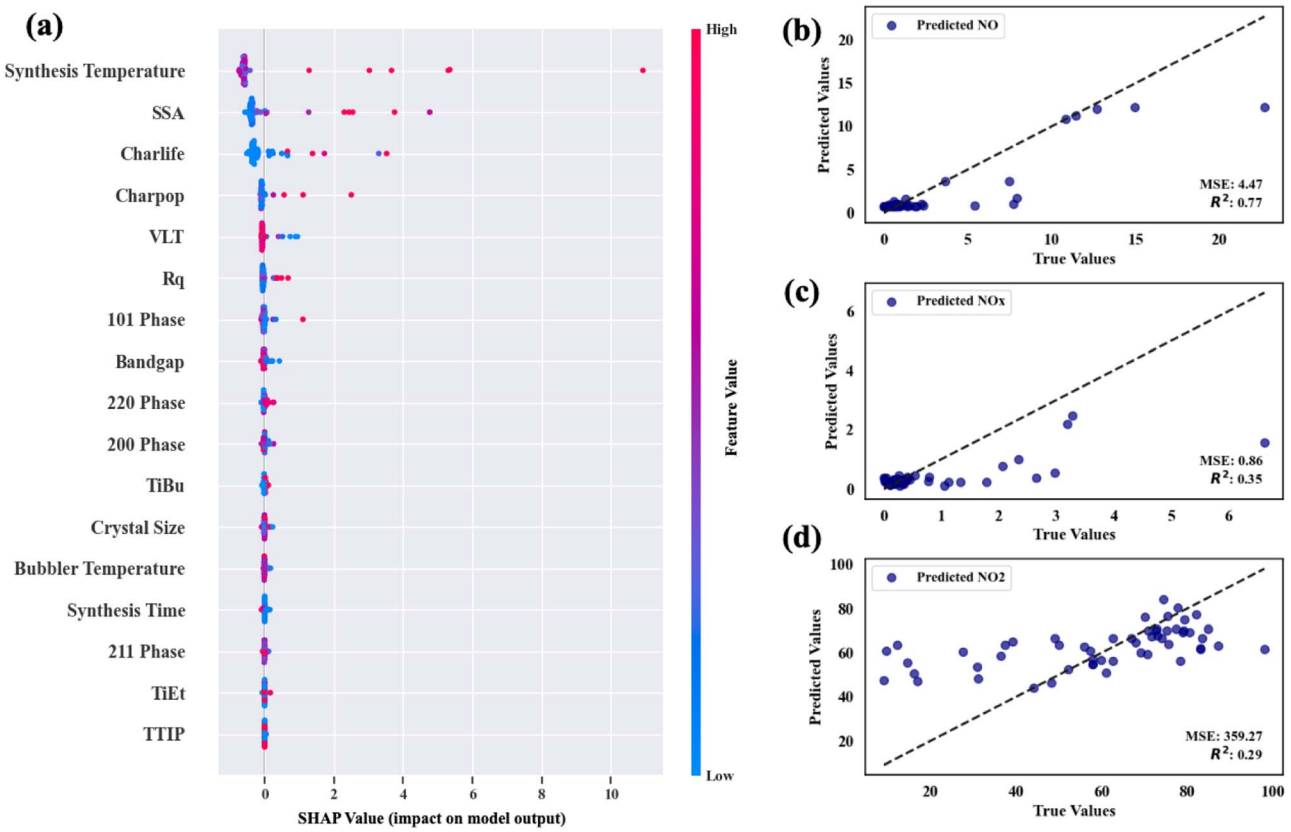

Fig. 9 (a) SHAP value for predicting photocatalytic NO conversion when applying the "modified property-prior prediction" strategy; experimental *versus* predictive value in simulations of (b) photocatalytic NO conversion, (c) photocatalytic NO_x conversion and (d) photocatalytic NO_2 selectivity.

samples with high NO conversion tend to be more opaque. These conclusions are consistent with those in our comparative experimental section and confirm the rationality and interpretability of our prediction model.

Moreover, the ML strategy also describes the importance of synthetic parameters in predicting photocatalytic NO activity. It is found that the model emphasizes the deposition temperature as a key factor affecting photocatalytic NO activity, where higher deposition temperatures usually lead to an increase in activity. The bubbler temperature and synthesis time during the synthesis are also major factors affecting the photocatalytic NO activity, whereas the selection of precursors has a relatively small impact on the results. This shows that the model suggests paying much attention to the control of deposition temperature, bubbler temperature and synthesis time in future production to enhance the NO conversion efficiency, while regulating the selection of precursors, however, might have a smaller contribution to improving the NO conversion.

The SHAP values of NO_x conversion and NO_2 selectivity predicted by the model can be found in Fig. S34.† It is noteworthy that the model emphasizes the contribution of crystal size and (101) crystal orientation to photocatalytic NO_x conversion and NO_2 selectivity, respectively. A higher crystal size helps to increase the overall conversion rate of NO_x, and the preferred orientation of the anatase (101) phase is negatively correlated with NO_2 selectivity. This indicates that increasing the anatase (101) phase can potentially reduce NO_2 selectivity in photocatalytic NO removal. This conclusion was not evident experimentally, and the reliability of this conclusion requires a deeper study.[73]

3.5.3 Industrial application and optimisation. Based on the existing data set and applying the best ML strategies, we simulated a total of 27 379 data points with different synthesis conditions (Fig. S35(b)–(d)†), in which TTIP, TiEt and TiBu were employed as precursors. The synthesis parameters encompassed a range of deposition temperatures from 350 to 600 °C (10 °C increments), bubbler temperatures from 100 to 220 °C (10 °C increments), and synthesis times from 1 to 27 min (1 min increments). All generated data, qualitatively speaking, were deemed reliable, as no negative values were predicted for any of the physicochemical properties and photocatalytic NO_x activity never outstripped NO activity.

Combining some of the most significant considerations for industrial applications of self-cleaning glass for photocatalytic NO_x remediation, we introduce a novel metric. This metric not only encompasses the photocatalytic NO activity, but also accounts for the product transparency and suppression of NO_2 production in the photocatalytic process.[62] The new metric denoted photocatalytic VLT × NO/NO_2, as expressed in eqn (12),

Table 4 Validation of ML predicted data and actual data with optimal samples under the new metric

Sample	NO conversion (%)	NO_x conversion (%)	NO_2 selectivity (%)	VLT (%)	Score from the new metric
Predicted TiEt_430_210_1	2.16	0.687	50.1	80	8636
Actual TiEt_430_210_1	0.412	0.361	8.19	77	2913
Commercial self-cleaning glass	0.274	0.178	34.8	77	1377

where [X] means the corresponding value derived from our simulated data, expressed in percentage terms:

$$\text{Metric}_{\text{VLT}\times\text{NO/NO}_2} = [\text{VLT}] \times [\text{NO}] \times (100\% - [\text{NO}_2]) \quad (12)$$

Here, higher values indicate a good balance between high conversion of NO species to HNO_3 and high transparency, which is often a requirement for glazing applications.[62]

Under this new metric, we can filter 5742 data points that meet the requirements of high transparency, where VLT $\geq$ 70. Among them, when using TiEt as the precursor, 3325 data points were seen, and when using TiBu as the precursor 2032 points were seen. The smallest number of data points of just 385 was observed when TTIP was used as the precursor. This shows that using TiEt is more likely to obtain products of high transparency for glazing applications.

For the optimal conditions predicted by our ML model, we synthesized a new coating, using the TiEt precursor as an example, to validate the precision of our ML-assisted optimisation. A picture of the new synthesized sample can be found in Fig. S35,† along with predictions. The results of the measured and predicted value are summarised in Table 4), and although the photocatalytic NO activity and NO_2 selectivity differed somewhat from the prediction, the VLT value was accurately predicted. Importantly, based on our metric, this sample ranked 3rd out of the other 12 samples produced in our study using TiEt which possess VLT > 70%, and showed a metric more than double that of a commercial self-cleaning glass.

Although there was a some deviation between the predicted values and outcomes for photocatalytic performances, this could mainly be attributed to the large error range in our NO_2 selectivity predictions. What should also be noted is that not all relevant physicochemical properties could be measured in our study, and fed into the ML model. For example, the conduction and valence band edge energy levels were not measured, which affect the ability of the material to drive the redox reactions that ultimately convert NO_x. On the other hand, our training data set was limited to 56 unique samples. Although the experimental data were reliable and of high quality, we understand that ML analysis is limited by this relatively small number of groups. One approach to improve our ML strategy would be to apply an iterative optimization approach, where one produces coatings based on optimal predictions from the current ML model, and then repeatedly inputs data from these new coatings back into the ML model to refine it. Alternatively, some optimization algorithms based on stochastic processes and Artificial Intelligence (AI) may result in more precise predictions, minimising the number of unique samples require to be produced and tested.[74]

4 Conclusion

This study involved the systematic study of the relationships between the synthesis parameters, physico-chemical properties and photocatalytic NO_x activity of TiO_2 coatings on glass produced by APCVD. Our analysis combined experimental methods with machine learning-assisted analysis, with the main conclusions of the study as follows:

1. 58 distinct TiO_2 coatings on glass were produced by systematically varying the synthesis parameters, with the most active coating produced using TiEt at a deposition temperature of 600 °C, a synthesis time of 3 minutes and a bubbler temperature of 160 °C. The sample showed a photocatalytic NO conversion efficiency of ~22.3% and a NO_x conversion efficiency of ~6.6%, with these values being 60-fold higher than those of a commercial self-cleaning glass.

2. The impacts of synthesis parameters on the physico-chemical properties and photocatalytic NO_x removal activity were qualitatively determined through our analysis of experimental results. It was found that the deposition temperature appeared to play the most influential role, with more active coatings produced at higher temperatures. In addition, a negative correlation between the material's optical properties, such as visible light transmittance and optical bandgap, and the photocatalytic NO and NO_x removal efficiency were also observed, whereas the surface roughness and photogenerated charge carrier kinetics of the sample were positively correlated with the sample photocatalytic NO and NO_x removal efficiency.

3. Two effective machine learning strategies were identified. Their accuracy and robustness in predicting the photocatalytic activity were rigorously evaluated and compared. The optimal strategy showed an excellent performance for predicting photocatalytic NO conversion (MSE = 4.87 and R^2 = 0.75). The SHAP value obtained by the optimal strategy revealed that the most influential factors for predicting the photocatalytic NO activity include sample surface roughness, carrier lifetime and visible light transmittance (VLT), while factors such as crystal properties and the optical bandgap have less of an impact. In terms of synthetic parameters, deposition temperature and bubbler temperature were identified as key synthesis parameters that control the photocatalytic activity. Importantly, these findings were highly consistent with our experimental observations.

4. Simulated data points were generated from our optimised ML model to identify synthesis conditions that meet the requirements of high transparency and the highest possible photocatalytic activity for the potential application of photocatalytic glazing for remediating NO_x pollution. The ML model was validated by producing a new sample in accordance with the predicted synthetic conditions. This new sample was found

to show comparatively high photocatalytic activity (ranking 3rd out of the 12 samples produced in our study using the same precursor that possessed similarly high transparency), whilst maintaining high visible light transmittance (77%). Moreover, it showed a photocatalytic NO_x removal activity near double that of a commercial self-cleaning glass.

In summary, this article is the first study to systematically explore the relationships between synthesis parameters, physicochemical properties and photocatalytic NO_x conversion efficiency of TiO_2 coatings using ML strategies. Importantly, we believe that this novel approach will not only provide guidance on the future production of TiO_2 coatings on window glass for photocatalytic NO_x remediation, but also showcases a more general approach to the optimisation of photocatalytic coatings that could be used for a range of processes.

Conflicts of interest

There are no conflicts to declare.

Acknowledgements

A. K. thanks the EPSRC for a Programme Grant (EP/W017075/1) and the Royal Society for an Equipment Grant (RSG/R1/180434). A. M. G. was supported by EPSRC Fellowship EP/T033231/1. Pilkington NSG are thanked for providing the Pilkington Optifloat™ float glass substrates. We also acknowledge the use of the EPSRC funded Physical Sciences Data-science Service hosted by the University of Southampton and STFC under grant number EP/S020357/1. Lee Tooley, Steve Atkins and Stefanos Karapanagiotidis are thanked for constructing and maintaining our chemical vapour deposition apparatus.

References

1 C. T. Bowman, *Symp. (Int.) Combust.*, 1992, **24**, 859–878.
2 L. Jaeglé, L. Steinberger, R. V. Martin and K. Chance, *Faraday Discuss.*, 2005, **130**, 407.
3 G. D. Oreggioni, F. M. Ferraio, M. Crippa, M. Muntean, E. Schaaf, D. Guizzardi, E. Solazzo, M. Duerr, M. Perry and E. Vignati, *Glob. Environ. Change*, 2021, **70**, 102350.
4 F. Rezaei, A. A. Rownaghi, S. Monjezi, R. P. Lively and C. W. Jones, *Energy Fuels*, 2015, **29**(9), 5467–5486.
5 K. Adil, K. Świrk, A. Zaki, A. H. Assen, G. Delahay, Y. Belmabkhout and A. Cadiau, *Energy Fuels*, 2022, **36**, 3347–3371.
6 S. Keav, S. Matam, D. Ferri and A. Weidenkaff, *Catalysts*, 2014, **4**, 226–255.
7 A. M. Beale, F. Gao, I. Lezcano-Gonzalez, C. H. F. Peden and J. Szanyi, *Chem. Soc. Rev.*, 2015, **44**, 7371–7405.
8 T. Selleri, A. D. Melas, A. Joshi, D. Manara, A. Perujo and R. Suarez-Bertoa, *Catalysts*, 2021, **11**, 404.
9 X. J. Liu, W. Xu, E. Z. Du, A. H. Tang, Y. Zhang, Y. Zhang, Z. Wen, T. X. Hao, Y. P. Pan, L. Zhang, B. Gu, Y. Zhao, J. L. Shen, F. Zhou, Z. L. Gao, Z. Feng, Y. H. Chang, K. Goulding, J. Collett, P. M. Vitousek and F. Zhang, *Philos. Trans. R. Soc., A*, 2020, **378**, 20190324.
10 *Research Handbook on EU Environmental Law*, ed. M. Peeters and M. Eliantonio, 2020, DOI: 10.4337/9781788970679.
11 B. A. Nault, J. L. Laughner, P. J. Wooldridge, J. D. Crounse, J. Dibb, G. Diskin, J. Peischl, J. R. Podolske, I. B. Pollack, T. B. Ryerson, E. Scheuer, P. O. Wennberg and R. C. Cohen, *Geophys. Res. Lett.*, 2017, **44**, 9479–9488.
12 J. A. Lasek and R. Lajnert, *Appl. Sci.*, 2022, **12**, 10429.
13 J. Chouhan and A. K. Chandrappa, *Innov. Infrastruct. Solut.*, 2023, **8**(90), 1–12.
14 P. Dong, N. Xu, Y. Xu and X. Wang, *Catal. Commun.*, 2016, **84**, 142–146.
15 D. Y. Shin, M. G. So and S. M. Han, *Mater. Sci. Forum*, 2006, **510–511**, 94–97.
16 H. Schwartz-Narbonne, S. H. Jones and D. J. Donaldson, *Environ. Technol. Lett.*, 2019, **6**, 92–97.
17 V. A. Maiorov, *Glass Phys. Chem.*, 2019, **45**, 161–174.
18 X. Zhang, R. Rao, B. Gao, S. Ma, F. Bi, C. Li, Z. Zhu, N. Liu, Y. Yang and Z. Wang, *Mater. Today Chem.*, 2023, **34**, 101755.
19 Z. Gao, L. Han, H. Gao, J. Chen, Z. Sun, C. Zhu, Y. Zhang, J. Shi, S. Chen and H. Wang, *J. Mater. Chem. A*, 2022, **10**, 12908–12920.
20 H. Khan and M. U. H. Shah, *J. Environ. Chem. Eng.*, 2023, **11**, 111532.
21 J. Lasek, Y.-H. Yu and J. C. Wu, *J. Photochem. Photobiol., C*, 2013, **14**, 29–52.
22 N. Serpone, *Catalysts*, 2018, **8**, 553.
23 G. Hüsken, M. Hunger and H. Brouwers, *Build. Environ.*, 2009, **44**, 2463–2474.
24 J. Ângelo, L. Andrade and A. Mendes, *Appl. Catal., A*, 2014, **484**, 17–25.
25 D. Wang, Z. Leng, M. Hüben, M. Oeser and B. Steinauer, *Constr. Build. Mater.*, 2016, **107**, 44–51.
26 Y. Wong, Y. Li, Z. Lin and A. Kafizas, *Appl. Catal., A*, 2022, **648**, 118924.
27 A. Jiamprasertboon, A. Kafizas, E. Hawkins, S. Singsen, T. Butburee, S. Wannapaiboon, W. Sangkhun, S. Nijpanich, T. Eknapakul, N. Chanlek, A. Waehayee, S. Suthirakun and T. Siritanon, *ACS Appl. Nano Mater.*, 2022, **6**, 738–749.
28 V. A. Ganesh, H. K. Raut, A. S. Nair and S. Ramakrishna, *J. Mater. Chem.*, 2011, **21**, 16304.
29 T. Minaai, K. D. Sanderson, Self-Cleaning Glass, In *Handbook of Self-Cleaning Surfaces and Materials*, Wiley, 2023, pp. 449–459, ch. 19, DOI: 10.1002/9783527690688.
30 M. Nolan, M. Pemble, D. Sheel and H. Yates, *Thin Solid Films*, 2006, **515**, 1956–1962.
31 R. Quesada-Cabrera, C. Sotelo-Vázquez, M. Quesada-González, E. P. Melián, N. Chadwick and I. P. Parkin, *J. Photochem. Photobiol., A*, 2017, **333**, 49–55.
32 M. Huang, S. Wang and H. Zhu, *J. Mater. Chem. A*, 2023, **11**, 21619–21627.
33 B. Oral, E. Can and R. Yildirim, *Int. J. Hydrogen Energy*, 2022, **47**, 19633–19654.
34 H. Mai, T. C. Le, D. Chen, D. A. Winkler and R. A. Caruso, *Chem. Rev.*, 2022, **122**, 13478–13515.
35 N. Goodarzi, Z. Ashrafi-Peyman, E. Khani and A. Z. Moshfegh, *Catalysts*, 2023, **13**, 1102.

36 A. Mills, A. Lepre, N. Elliott, S. Bhopal, I. P. Parkin and S. O'Neill, *J. Photochem. Photobiol., A*, 2003, **160**, 213–224.
37 A. L. Patterson, *Phys. Rev.*, 1939, **56**, 978–982.
38 V. Diesen, M. Jonsson and I. P. Parkin, *Chem. Vap. Deposition*, 2013, **19**, 355–362.
39 R. Swanepoel, *J. Phys. E: Sci. Instrum.*, 1983, **16**, 1214–1222.
40 J. Tauc, *Mater. Res. Bull.*, 1968, **3**, 37–46.
41 H. K. Abbood and N. A. Ali, *J. Opt.*, 2023, DOI: **10.1007/s12596-023-01393-6**.
42 N. Negishi, K. Takeuchi and T. Ibusuki, *Appl. Surf. Sci.*, 1997, **121–122**, 417–420.
43 X. Wang, A. Kafizas, X. Li, S. J. A. Moniz, P. J. T. Reardon, J. Tang, I. P. Parkin and J. R. Durrant, *J. Phys. Chem. C*, 2015, **119**, 10439–10447.
44 A. Kafizas, X. Wang, S. R. Pendlebury, P. Barnes, M. Ling, C. Sotelo-Vazquez, R. Quesada-Cabrera, C. Li, I. P. Parkin and J. R. Durrant, *J. Phys. Chem. A*, 2016, **120**, 715–723.
45 A. Mills, R. Andrews, R. Han, C. O'Rourke and S. Hodgen, *J. Photochem. Photobiol., A*, 2020, **400**, 112734.
46 F. Pedregosa, G. Varoquaux, A. Gramfort, V. Michel, B. Thirion, O. Grisel, M. Blondel, P. Prettenhofer, R. Weiss, V. Dubourg, J. Vanderplas, A. Passos, D. Cournapeau, M. Brucher, M. Perrot and E. Duchesnay, *J. Mach. Learn. Res.*, 2011, **12**, 2825–2830.
47 A. Dunn, Q. Wang, A. Ganose, D. Dopp and A. Jain, *npj Comput. Mater.*, 2020, **6**(1), 138.
48 G. Varoquaux, P. R. Raamana, D. A. Engemann, A. Hoyos-Idrobo, Y. Schwartz and B. Thirion, *NeuroImage*, 2017, **145**, 166–179.
49 G. Hyett, M. Green and I. P. Parkin, *J. Am. Chem. Soc.*, 2006, **128**, 12147–12155.
50 A. Kafizas, C. Crick and I. P. Parkin, *J. Photochem. Photobiol., A*, 2010, **216**, 156–166.
51 M. N. Field, *Atmospheric Pressure Chemical Vapour Deposition of Vanadium, Chromium and Titanium Oxides*, 2002, p. 139.
52 Y. M. Abdulraheem, S. Ghoraishi, L. Arockia-Thai, S. K. Zachariah and M. Ghannam, *Adv. Mater. Sci. Eng.*, 2013, **2013**, 574738.
53 E. Kraleva, M. L. Saladino, R. Matassa, E. Caponetti, S. Enzo and A. Spojakina, *J. Struct. Chem.*, 2011, **52**, 330–339.
54 A. Kania, M. M. Szindler and M. Szindler, *Coatings*, 2021, **11**, 70.
55 J. G. Choi and K. Y. Park, *J. Nanopart. Res.*, 2006, **8**, 269–278.
56 Y. Guo, X. wen Zhang and G. rong Han, *J. Mater. Sci. Eng. B*, 2006, **135**, 83–87.
57 K. Möls, L. Aarik, H. Mändar, A. Kasikov, A. Niilisk, R. Rammula and J. Aarik, *Opt. Mater.*, 2019, **96**, 109335.
58 M. M. Hasan, A. S. M. A. Haseeb, R. Saidur and H. H. Masjuki, *Int. J. Mech. Eng.*, 2008, **2**, 410–414.
59 S. A. O'Neill, I. P. Parkin, R. J. H. Clark, A. Mills and N. Elliott, *J. Mater. Chem.*, 2002, **13**, 56–60.
60 S. Krumdieck, R. Gorthy, A. J. Gardecka, D. Lee, S. S. Miya, S. D. Talwar, M. I. Polson and C. Bishop, *Surf. Coat. Technol.*, 2017, **326**, 402–410.
61 H. H. Ku, *Notes on the Use of Propagation of Error Formulas*, 1965.
62 J. Z. Bloh, A. Folli and D. E. Macphee, *RSC Adv.*, 2014, **4**, 45726–45734.
63 H. Kim, J. An, S. Maeng, J.-S. Shin, E. Choi and J.-Y. Yun, *Materials*, 2022, **15**, 3021.
64 D. C. Bradley and J. D. Swanwick, *J. Chem. Soc.*, 1958, 3207.
65 J. Aarik, A. Aidla, V. Sammelselg, T. Uustare, M. Ritala and M. Leskelä, *Thin Solid Films*, 2000, **370**, 163–172.
66 P. Chin and D. F. Ollis, *Catal. Today*, 2007, **123**, 177–188.
67 Y. Quan, M. H. N. YiO, Y. Li, R. J. Myers and A. Kafizas, *J. Photochem. Photobiol., A*, 2023, **443**, 114889.
68 T. Choi, J.-S. Kim and J. H. Kim, *Adv. Powder Technol.*, 2016, **27**, 347–353.
69 K. Eufinger, D. Poelman, H. Poelman, R. De Gryse and G. Marin, *Thin Solid Films*, 2008, **37661**, 2.
70 R. Scheda and S. Diciotti, *Appl. Sci.*, 2022, **12**, 6681.
71 W. E. Marcilio and D. M. Eler, *2020 33rd SIBGRAPI Conference on Graphics, Patterns and Images (SIBGRAPI)*, 2020.
72 S. M. Lundberg, G. Erion, H. Chen, A. DeGrave, J. M. Prutkin, B. Nair, R. Katz, J. Himmelfarb, N. Bansal and S.-I. Lee, *Nat. Mach. Intell.*, 2020, **2**, 56–67.
73 P. Guo, X. Fu, P. Deák, T. Frauenheim and J. Xiao, *J. Phys. Chem. Lett.*, 2021, **12**, 7708–7716.
74 Y. Wu, A. Walsh and A. Ganose, *ChemRxiv*, preprint, 2023, DOI: **10.26434/chemrxiv-2023-l8sms**.